Available online at www.sciencedirect.com

ScienceDirect

Geochimica et Cosmochimica Acta 293 (2021) 127–141

Geochimica et Cosmochimica Acta

www.elsevier.com/locate/gca

Reduction of uranyl and uranyl-organic complexes mediated by magnetite and ilmenite: A combined electrochemical AFM and DFT study

YoungJae Kim [1], Maria C. Marcano, Sooyeon Kim, Udo Becker *

Department of Earth and Environmental Sciences, University of Michigan, 1100 North University Ave., Ann Arbor, MI 48109-1005, USA

Received 21 April 2020; accepted in revised form 13 October 2020; available online 21 October 2020

Abstract

Reduction of mobile aqueous uranyl complexes can be hindered by the strength of the uranyl-ligand complex and the resistivity of the complexes to electron transfer. Semiconducting solids, such as magnetite (Fe_3O_4) and ilmenite ($FeTiO_3$), can facilitate otherwise-slow electron transfer between the reductant and oxidant, especially if these species are adsorbed on their surfaces as inner-sphere complexes. Electrons can then be shuttled through the surface or the structure. This process can be facilitated by either finding a new electron transfer path or by weakening or destroying the ligand-uranyl complex.

Using *in situ* electrochemical atomic force microscopy (EC-AFM), we imaged reduction products of uranyl as mediated by magnetite and ilmenite in the absence or presence of the organic ligands, ethylenediaminetetraacetate (EDTA) and oxalate. *In situ* images of uranyl reduction show gradual nucleation and growth of reduced uranium on the mineral surfaces with decreasing reduction potentials. X-ray photoelectron spectroscopy (XPS) measurements indicate pentavalent uranium as the dominant uranium species resulting from uranyl reduction mediated by magnetite and ilmenite. The reduction potentials of uranyl-organic species relevant to our reaction system, $(U^{VI}O_2{\cdot}oxalate)^0$ and $(U^{VI}O_2{\cdot}HEDTA)^-$, are derived using quantum–mechanical modeling and compared with the midpoint potentials obtained from cyclic voltammetry measurements. The spectroscopic, electrochemical, and computational data suggest that the catalysis of Fe-bearing minerals facilitates the reduction of uranyl-organic complexes. U(VI)-oxalate complexes are redox-active and participate directly in the reduction mediated by magnetite. In the presence of EDTA, reduction of uranyl may proceed in concert with ligand exchange between metals (i.e., U and Fe) on the mineral surface. The proposed mechanism is the breaking of uranyl-organic bonds upon interaction with the mineral surface followed by the formation of Fe-organic bonds, thereby allowing the reduction of hexavalent uranyl to pentavalent one.

© 2020 Elsevier Ltd. All rights reserved.

Keywords: Uranyl reduction; Oxalate; Ethylenediaminetetraacetate (EDTA); Magnetite; Ilmenite; Atomic Force Microscopy (AFM); Density Functional Theory (DFT)

1. INTRODUCTION

Magnetite (Fe_3O_4) and ilmenite ($FeTiO_3$) are the two most common ferrous iron-containing oxide minerals in the Earth's crust. Weathering processes involving these minerals provide electrons and Fe atoms to the aqueous and subsurface environments due to their thermodynamic

* Corresponding author.
E-mail addresses: youngjkm@umich.edu (Y. Kim), ubecker@umich.edu (U. Becker).
[1] Present address: Chemical Sciences and Engineering Division, Argonne National Laboratory, Argonne, IL 60439, USA.

https://doi.org/10.1016/j.gca.2020.10.016
0016-7037/© 2020 Elsevier Ltd. All rights reserved.

instability under ambient (oxic) geochemical conditions (White et al., 1994). This iron cycling is coupled with the cycling of O_2, carbon, and redox-sensitive elements (e.g., Se, Cr, and U) in sediments, soils, and groundwater. Magnetite and ilmenite can facilitate or catalyze otherwise-slow electron transfer reactions between a reductant and an oxidant where these redox species are adsorbed on oxide surfaces. In addition to both minerals acting as Fe sources, their surfaces contribute to the dehydration of redox-active species, and their semiconducting properties aid in the actual electron-transfer. In such catalysis processes, electrons can be shuttled through the mineral surface or the mineral structure (see the excellent review by Xu and Schoonen (2000) and references therein).

The reduction of actinide ions mediated by iron-bearing minerals such as magnetite, hematite, and pyrite has been the subject of considerable research (e.g., Powell et al., 2004; Hixon et al., 2010; Renock et al., 2013; Taylor et al., 2015; Yuan et al., 2015a, 2015b; Pan et al., 2017; Taylor et al., 2017a, 2017b), while similar abiotic redox reactions mediated by ilmenite have not been reported yet. The uranyl ion (UO_2^{2+}) is the most stable form of uranium with the oxidation number VI in oxic natural settings such as soils and groundwater. Various processes, including sorption onto minerals, secondary mineralization as well as reduction into immobile forms can impede the mobility of uranyl (e.g., Sun et al., 2014; Kim et al., 2015; Pan et al., 2017; Yang et al., 2020). It has long been thought that biotic and abiotic reduction of uranyl results in uranium oxides with the primary oxidation state of IV (Lovley, 1993; Wersin et al., 1994; O'Loughlin et al., 2003). Recent spectroscopic studies, however, reveal the stability of U(V) as a product of uranyl reduction as mediated by iron-bearing minerals (Ilton et al., 2012; Renock et al., 2013; Yuan et al., 2015a). Ilton et al. (2012) studied the reduction of U(VI) incorporated in the structure of hematite in the presence of organic reductants. Their results reveal that structurally-incorporated U(VI) is reduced to U(V), whereas the non-incorporated proportion of U(VI) is reduced to U(IV). Renock et al. (2013) adopted an electrochemical setup that involves Fe-bearing minerals, including pyrite, hematite, and magnetite as the working electrode. They suggested a two-step U(VI) reduction mechanism in which (1) electron transfer leading to the formation of U(V) is followed by (2) a disproportionation reaction forming U(IV) and U(VI). Yuan et al. (2015a) reported spectroscopic evidence of one-electron transfer between U(VI) and U(V) as mediated by magnetite, which results in U(VI)/U(V) mixed solids as a final product of uranyl reduction. These studies suggest that abiotic redox transformation from U(VI) to U(V) can be mediated by semiconducting minerals. It is expected that uranium species and solids containing pentavalent U may be produced as (meta-) stable intermediates or products during redox reactions in natural settings.

The formation of complexes with inorganic (e.g., carbonates) and organic ligands plays a critical role in determining the geochemical behavior of uranyl besides the redox chemistry of U. The complexation can increase the stability of dissolved uranyl species and slow down electron transfer processes. Oxalic acid is a natural source of protons and metal-complexing organic ligands that can increase metal (bio-)availability in various ecosystems (Gadd, 1999). Moreover, oxalate can form in nuclear waste repositories through the decomposition of other organic compounds (Campbell et al., 1994). Ethylenediaminetetraacetate (EDTA) is a metal-chelating agent commonly used to increase the solubility of toxic elements like U as required for industrial purposes such as chemical cleaning and decontamination operations. Since uranyl forms strong bonds with these organic molecules, metal–ligand interactions are essential in evaluating redox reactions in solutions and on mineral surfaces, and consequently, the mobility of uranyl in aqueous systems (Havel et al., 2002).

Atomic force microscopy (AFM) has been a powerful tool to visualize and characterize geochemically relevant reactions at atomic, nanometer, or micrometer scales. Especially *in situ* AFM analysis is useful to investigate the growth and dissolution mechanisms and kinetics of sparingly soluble minerals (e.g., calcite and barite; Pina et al., 1998, 2004; Risthaus et al., 2001; Becker et al., 2002) as well as the surface sorption and reactivity of organic/inorganic species on oxide and clay minerals (Iwasawa et al., 1999; Charlet et al., 2002; Hemmersam et al., 2008; Karlsson et al., 2010). Only a few recent studies have addressed the progress of a metal reduction/precipitation reaction mediated by semiconducting minerals based on *in situ* AFM analysis combined with electrochemical methods (EC-AFM). Yuan et al. (2015a) were the first to use this technique to visualize uranyl reduction as catalyzed by magnetite with the redox potential exerted on the adsorbed uranyl being controlled by applying an electrochemical potential on the mineral electrode. The results demonstrated that there is instantaneous growth of U(VI)/U(V) mixed oxides as the uranyl reduction proceeds to reducing conditions. Walker et al. (2016) observed Cr(VI) reduction to Cr(III) mediated by the magnetite substrate as a function of Eh and pH. Their AFM analysis combined with spectroscopic data suggest the intimate growth of Cr- and Fe-bearing particles like chromite ($FeCr_2O_4$) on the mineral substrate as reduced Cr is diffused to or incorporated into the magnetite surface. *In situ* AFM analysis is a promising technique to characterize redox reactivity of semiconducting minerals and nucleation mechanisms of redox-sensitive elements.

The main objective of this study is to integrate electrochemical and microscopic approaches to understand reaction mechanisms and pathways of the uranyl reduction and nucleation mediated by magnetite and ilmenite. For this purpose, an electrochemical set that involves the mineral electrode as the working electrode is used to simulate oxidation and reduction of uranium species as a function of redox potential. We imaged reduction of uranyl in the absence and presence of organic compounds using an *in situ* AFM setup and analyzed spectroscopic and electrochemical data to examine whether reduction of hydrated uranyl and uranyl-organic complexes can be facilitated by Fe-bearing minerals. The reduction potentials of uranyl-organic species are evaluated using quantum–mechanical

modeling and compared with the midpoint potentials measured with the mineral electrodes. By evaluating mechanisms and pathways of heterogeneous redox reactions involving a mineral, this study intends to advance our understanding of redox transitions of complexed actinyl ions and catalytic effects of Fe-bearing minerals in subsurface environments.

2. METHODS

2.1. Mineral electrodes and reagents

The magnetite samples used in this study are octahedral–dodecahedral crystals collected from Mineville, New York, and the Itabira District, Minas Gerais, Brazil (Ward's Science, USA). Minor amounts of titanium and aluminum were measured using energy-dispersive x-ray spectroscopy (EDS). The ilmenite specimens used in this study were sourced from St. Urbain, Canada (Ward's Science, USA), and XRD and SEM analyses (not shown here) reveal intergrowth of ilmenite with hematite, which was reported by a previous study (Gillson, 1932). The crystals were cut using a water-saw and polished with silicon carbide paper (grit sizes 320, 800, 1500, 3000, and 4000). The samples were then sonicated for 10 min and rinsed with Milli-Q® water (resistivity, 18.2 MΩ·cm; TOC < 5 ppb) to remove any contaminants introduced during polishing. The exposed areas of the final samples were approximately 1.0 to 2.0 cm^2.

Stock solutions of uranyl and organic compounds were prepared using Milli-Q® water and uranyl nitrate hexahydrate ($UO_2(NO_3)_2$·$6H_2O$, International Bio-analytical Industries; purity, 98–102%), disodium EDTA dihydrate ($C_{10}H_{14}N_2Na_2O_8$·$2H_2O$, Fisher Chemical, 99.0 to 101.0%), oxalic acid dihydrate ($C_2H_2O_4$·$2H_2O$, Baker Analyzed; 99.5 to 102.5%), and ferrous sulfate heptahydrate ($FeSO_4$·$7H_2O$, Fisher Chemical; ≥ 99.0%).

2.2. Solution chemistry

For all experiments, the concentration of uranyl was 0.3 or 0.5 mM, and the solution was adjusted to a pH of 3.0 by adding concentrated HCl or NaOH. The same concentrations of organic compounds and uranyl were added, unless stated otherwise, which corresponds to a uranyl/organic-compound molar ratio of 1:1. Acidic conditions were necessary to prevent wet precipitation of uranyl solids. The uranyl/organic ratio was chosen to maximize the visualization of uranyl nucleation in the AFM measurement. Specifically, upon AFM imaging, uranium nucleation was found to be less pronounced with higher concentrations of organic compounds. Prior to electrochemical and AFM experiments, 10 ml of the solution was purged with N_2 for 10 min to minimize the presence of oxygen and carbon dioxide, and a N_2 atmosphere was maintained throughout each experiment.

For our experimental conditions, aqueous U(VI) species and saturation index with respect to various solid phases were calculated by Visual MINTEQ ver. 3.0 with the Thermo.vdb database (Table 1). Under our experimental conditions (pH 3.0; [UO_2^{2+}], [org] = 0.3 mM), 89% and 93% of the U speciation is accounted for by U-organic complexes, including ($U^{VI}O_2$·HEDTA)$^-$ and ($U^{VI}O_2$·oxalate)^0, as the main species in solution containing EDTA and oxalate, respectively (Table 1).

2.3. Electrochemical AFM experiments

The experimental setup within the AFM fluid cell consists of a three-electrode configuration in which magnetite and ilmenite serve as the working electrode, with a platinum wire as the counter electrode and a silver wire as the quasi-reference electrode (+250 mV vs. the standard hydrogen electrode, SHE). In this electrochemical cell (Bruker Corporation, Santa Barbara, California; for an illustration, see Fig. A1, Appendix A, in Walker et al., 2016), the mineral samples were affixed flat on an etched Teflon® disk using Torr Seal® low vapor pressure epoxy. The Teflon disk was then mounted to the base of the AFM fluid cell, and electrical contact was established with a spring through a small opening in the disk.

The redox potential was controlled using a CHI 760D potentiostat, and EC-AFM experiments were performed using an in-house Dimension Icon atomic force microscope (Bruker). The Eh investigated ranged from +1.15 to −0.65 V (+0.9 to −0.9 V vs. Ag/AgCl electrode). Cyclic voltammetry was performed using the mineral electrode, and collected data were analyzed to identify specific redox species responsible for electrical signals at given pH and Eh values.

Peak Force Tapping (PFT) mode experiments were performed in fluid using silicon nitride tips (DNP, nom. Frew. 23 kHz, nom. Spring constant 0.12 N/m). In PFT, developed by Bruker, the tip makes intermittent contact with the sample surface. Scratches and grooves produced when polishing the surface can serve as reference features during the experiment. After acquired, images were cleaned and flattened using the NanoScope Analysis® software version 2.0 (Bruker).

Table 1
Uranyl speciation calculated for aqueous uranyl solution with oxalate and EDTA at pH 3.0 ([UO_2] and [org.] = 0.3 mM).

	In the presence of oxalate		
	UO_2^{2+}	(UO_2·oxalate)^0	(UO_2·$oxalate_2$)$^{2-}$
Molar fraction	0.06	0.93	<0.01
	In the presence of EDTA		
	UO_2^{2+}	(UO_2·HEDTA)$^-$	((UO_2)$_2$·EDTA)^0
Molar fraction	0.11	0.75	0.14

2.4. Material characterization

XPS analysis was performed using a Kratos Axis Ultra spectrometer with monochromatic and focused Al Kα radiation (1486.6 eV). The x-ray emission anode voltage and current applied during spectra acquisition were 14 keV and 8 mA, respectively. Pass energies of 160 and 20 eV were used on survey and core scans, respectively. All measurements were performed with a hybrid lens and slot aperture ($700 \times 300\ \mu m^2$) under ultra-high vacuum conditions ($<10^{-8}$ Torr). Spectra were analyzed using the CASA XPS software (version 2.3.16, www.casaxps.com), and binding energies were calibrated to the C 1s peak (284.9 eV). Caution should be taken on XPS analysis of U because the X-ray beam is likely to induce reduction of U(VI) during the measurement (Ilton et al., 2007). For each specimen, sequential analyses were performed on the same spot in order to examine the possibility of beam-induced reduction, as previously reported by Ulrich et al. (2009). Specimens obtained from reaction with EDTA and oxalate were stable over the first several spectra. All XPS spectra presented in this study were collected from the first two scans in each measurement to minimize the contribution of beam-induced reduction.

2.5. Molecular structure and energy calculation

The Gaussian 09 package was used to model the atomic structures of hydrated uranyl with and without organic ligands based on molecular orbital calculation. All calculations were performed using the DFT-HF hybrid B3LYP density functional (Lee et al., 1988). Relativistic effects for U were included in the calculation using pseudopotentials and basis set information (Stuttgart RSC 1997) collected from the EMSL Basis Set library. Energy-consistent pseudopotentials and basis sets for the C, O, and N atoms (ECP2MWB) were adopted from the Stuttgart/Cologne Group library (Bergner et al., 1993; www.tc.uni-koeln.de). The 6-31++G** basis is used to treat the H atoms in the calculations.

Cluster models of uranyl species (as UO_2^{2+} and UO_2^{+}) and their complexes with organic ligands (oxalate and EDTA) were constructed and serve as the basis for investigation of electron exchange reactions between these species. All reactions are assumed to occur in the water solvent such that hydration is an essential parameter in this reaction system. All models include explicit water molecules that comprise the first and second hydration spheres. Solvation effects are further included using the conductor-like polarizable continuum model (CPCM) as implemented in Gaussian 09. This model accounts for the contribution of higher-order spheres of hydration within a homogeneous dielectric fluid around the first and/or second coordination environment(s).

3. RESULTS

3.1. Cyclic voltammetry of uranyl

Cyclic voltammetry (CV) was used to evaluate the thermodynamics of redox processes mediated by magnetite and ilmenite in aqueous solutions. The pseudocapacitance of magnetite and ilmenite originates from the redox transformation between ferrous and ferric iron adsorbed on the surfaces. Since this chemical process results in large currents over the range of potentials used, CV measurements were performed with the blank (i.e., NaCl only) and uranium solutions (U(VI) + NaCl), separately (Figs. 1A and 2A). The data were compared to distinguish electric signals of redox-active species from those of the mineral working electrodes. CV analyses were also performed with solutions containing oxalate or EDTA to examine the effects of the organic ligands on uranium redox transformation (Figs. 1B, C, and 2B). The first step for this evaluation is to identify cathodic and anodic peaks that represent the reduction and oxidation of a redox-sensitive species.

On the cyclic voltammogram, the midpoint potential, $E_{mid} = (E_{pa} + E_{pc})/2$, can be defined from anodic and cathodic peak positions, E_{pa} and E_{pc}, respectively. E_{mid} values can be compared with thermodynamically defined standard reduction potentials (E^0) to assign CV peaks to specific redox reactions unless the peak positions are hard to be defined (e.g., due to peak broadness) or the activities of the oxidized and reduced species are not known.

One pair of anodic and cathodic peaks appears at +0.27/−0.05 V in cyclic voltammograms of U(VI) solutions measured with magnetite (Fig. 1A) with a midpoint potential of +0.11 V. This value is close to the standard reduction potential of the reversible reduction of U(VI) to U(V) ($E^0 =$ +0.16 V vs. SHE; Eq (1)) and consistent with commonly reported values of this redox transformation that range from +0.05 to +0.15 V vs. SHE (Djogić and Branica, 1993; Renock et al., 2013).

$$U^{VI}O_2^{2+} + e^- \leftrightarrow U^{V}O_2^{+} \quad (1)$$

In the presence of oxalate (U/oxalate molar ratio = 1:1), one pair of anodic and cathodic peaks is measured at +0.2/−0.14 V with a midpoint potential of +0.03 V (Fig. 1B). The peak shift of U(VI)/U(V) redox transformation by about 0.1 V with respect to the reduction potential of hydrated uranyl (Eq. (1)) is attributed to the complexation of uranyl with oxalate (Eq. (2); the potential shift $\Delta E^0 = +0.06$ V is the quantum-mechanically derived potential-shift approximation described in Section 3.4).

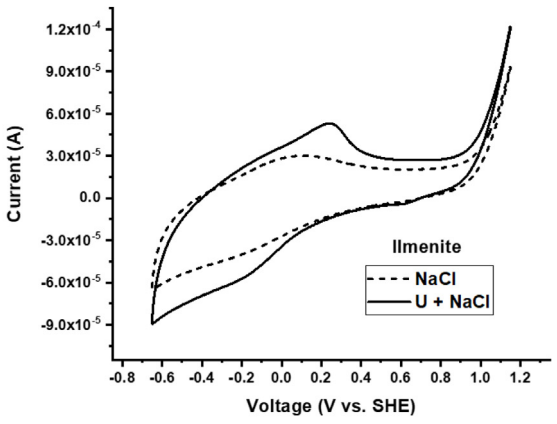
$$(U^{VI}O_2{\cdot}\text{oxalate})^0 + e^- \leftrightarrow (U^{V}O_2{\cdot}\text{oxalate})^- \quad (2)$$

In the CV curve measured using the magnetite electrode in solution containing U and EDTA (1:1 molar ratio, Fig. 1C), a pair of anodic and cathodic peaks appears at 0.26/−0.03 V and the midpoint potential is +0.12 V, which is close to the potential of the U(VI/V) reduction (Eq. (1)). Since U-EDTA complexes are the main uranyl species in this solution (Table 1), it should be examined whether the U-EDTA species contribute to the peak pair (Eq. (3); calculated $E^0 = -0.22$ V vs. SHE).

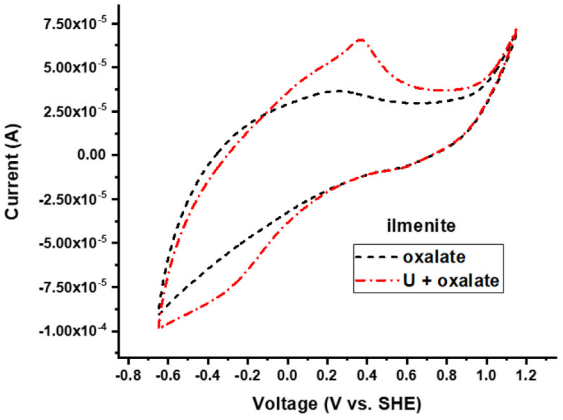
$$(U^{VI}O_2{\cdot}\text{HEDTA})^- + e^- \leftrightarrow (U^{V}O_2{\cdot}\text{HEDTA})^{2-} \quad (3)$$

The contributions of U-organic complexes to U redox transformation mediated by magnetite is further examined using first-principles calculations of shifts in the U reduction potential by organic complexation (see Section 3.4).

The measurement with ilmenite in uranyl solution (Fig. 2A) reveals an anodic/cathodic peak pair at 0.25/−0.15 V and a midpoint potential of +0.05 V. The CV measurement in solution containing uranyl and oxalate at a 1:1 molar ratio (Fig. 2B) shows a pair of anodic and cathodic peaks at 0.35/−0.25 V whose midpoint potentials are approximately +0.05 V. Upon CV with ilmenite, accurate measurement of reduction potentials using midpoint potentials is limited by the fact that the cathodic peaks are less sharp than the anodic peaks.

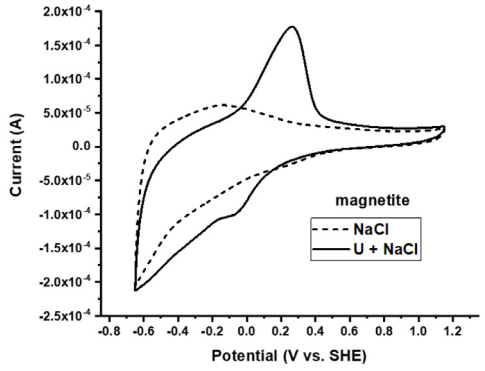


A

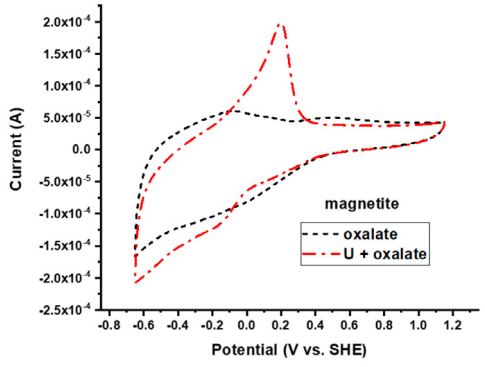


B

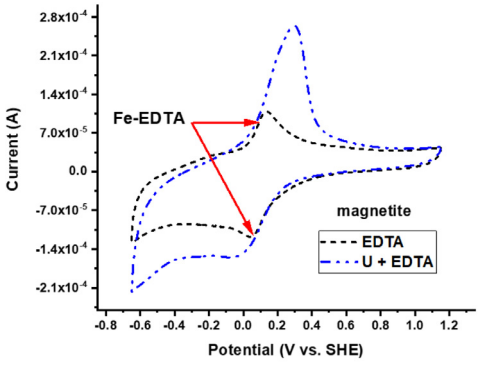
Fig. 2. Cyclic voltammograms for U(VI) measured using the ilmenite working electrode. Comparison between the U(VI)-containing and blank solutions with (A) no organic ligands and (B) oxalate (all solutions contained 0.1 M NaCl as a background electrolyte; $[UO_2^{2+}] = 0.5$ mM; [oxalate] = 0.5 mM).



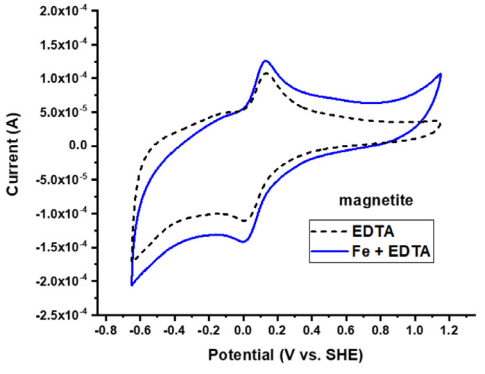
A



B



C



D

Fig. 1. Cyclic voltammetry (CV) measured using the magnetite working electrode. Comparison between the U(VI)-containing and blank solutions with (A) no organic ligands, (B) oxalate, and (C) EDTA ($[UO_2^{2+}] = 0.5$ mM; [Org.] = 0.5 mM). (D) Comparison between the Fe(II)-containing and blank solutions with EDTA ([Fe] = 0.5 mM; [EDTA] = 0.5 mM). All solutions contained 0.1 M NaCl as a background electrolyte.

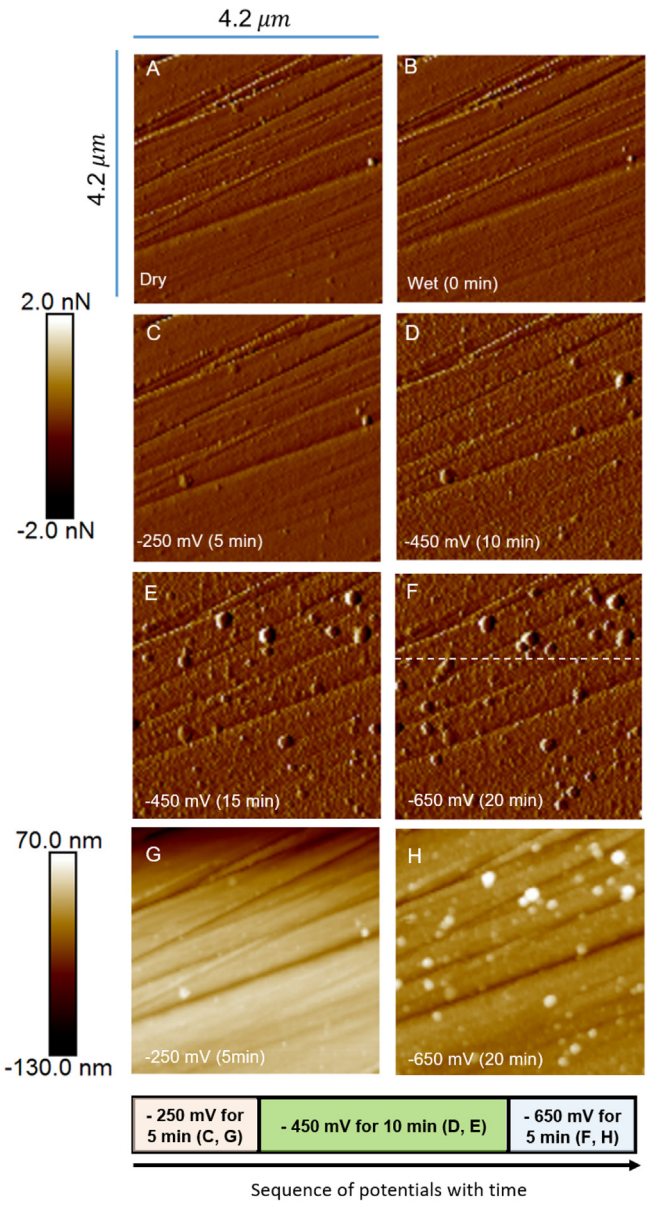


Fig. 3. EC-AFM peak force error (PFE) images (A–F) and height images (G and H) as a function of electric potentials applied. The electrode was a substrate of ilmenite immersed in a solution with 0.5 mM uranyl at pH 3.0. Cumulative times elapsed during the potential sequence are shown on the images. The white dashed line in (F) represents a cross-section selected for measuring surface topography as a function of potential (see Fig. 5A).

3.2. The growth of reduced U solids on magnetite and ilmenite

The mineral surface was first imaged in the absence of an applied potential before and after the addition of fluids containing uranyl (Figs. 3A and B and 4A). The main purpose of this step is to survey the substrate before any electrochemical interaction takes place and determine if sorption occurs at the open circuit potential (OCP). The resulting images were used to compare with growth features that appear on the surface as a function of potential. After taking the baseline images, the ilmenite and magnetite electrodes were polarized at specific electrochemical potentials (−250, −450, and −650 mV vs. SHE). Variations on the ilmenite and magnetite surfaces were recorded in the sequence of decreasing potentials, which simulates progressively-reducing conditions at the mineral-fluid interface (Figs. 3 and 4).

At the OCP, the ilmenite surface shows no distinct changes between the images acquired before and after adding the solution to the reaction cell (Fig. 3A and B), ensuring that no precipitation occurs solely by solution chemistry. The surface characteristics change with the applied potential: At −250 mV, sorbates begin to appear on the ilmenite surface within the first 5 min of polarization. In general, these growing particles are 200 nm or less

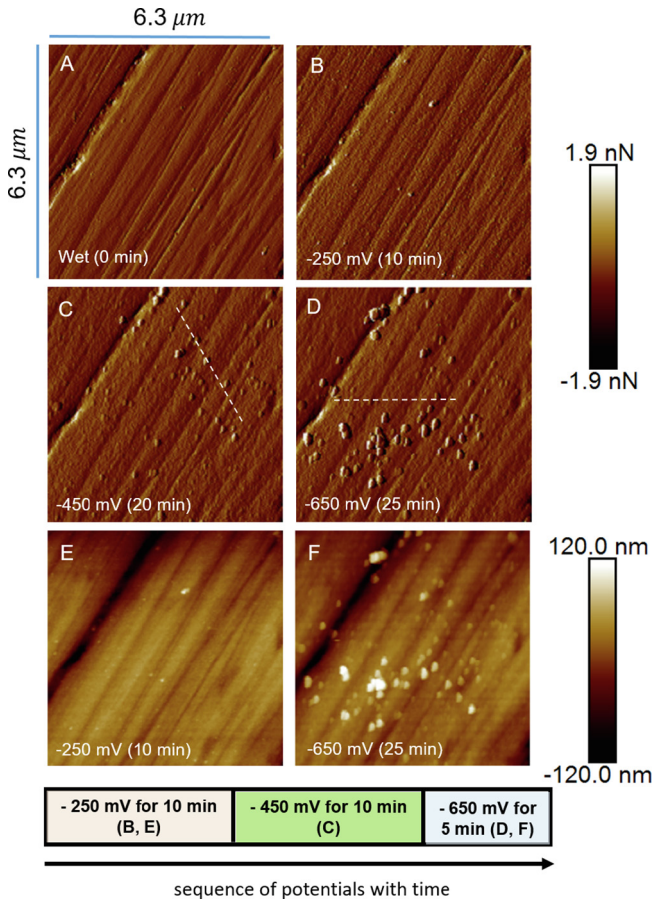


Fig. 4. EC-AFM peak force error (PFE) images (A to D) and height images (E and F) as a function of electric potentials applied. The electrode was a substrate of magnetite immersed in a solution with 0.5 mM uranyl at pH 3.0. Cumulative times elapsed during the potential sequence are shown on the images. The white dashed lines (C and D) represent cross-sections over which surface topography is measured (see Fig. 5B).

in size (measured in the longest dimension) and angular or irregular in shape. The number of particles increases drastically, while the potential is held at −450 mV for 5 to 10 min (compare Fig. 3D and E). After 5 min of polarization at −250 mV and 10 min at −450 mV, the growth of some sorbates is completed, resulting in particles with a circular base (Fig. 3E). During the 5 min polarization at −650 mV, the growth rate of particles in size and number slows down, and the surface is nearly saturated with sorbates (Fig. 3F and H). The size of the nuclei averages 100 nm, reaching a maximum of 230 nm. The change in depth profiles of the ilmenite surface as a function of potential is presented in Fig. 5A. The surface topographic features are changed the most upon the transition from −250 to −450 mV. At −450 and −650 mV, the adsorbate changes less and the cross-sections of the U sorbates appear bell-shaped with heights of 50–100 nm.

On the magnetite surface, the image taken at OCP does not reveal the growth of adsorbate after adding uranyl solution (Fig. 4A). Only a few sorbates are visible on the $6.3 \times 6.3\ \mu m^2$ magnetite surface during the first 10 min polarization at −250 mV (Fig. 4B). A drastic increase in the number of nuclei is observed after 10 min polarization at −450 mV (Fig. 4C). These nuclei are less than 100 nm long at this stage. Upon the polarization at −650 mV, the preexisting nuclei barely grow further, whereas new nuclei rapidly grow in 5 min (Fig. 4D). This is probably because the surface reactive sites where the preexisting nuclei grew were fully occupied with U precipitates before the polarization. In general, rapidly grown sorbates at −650 mV are a mixture of angular and round particles, and the size of the nuclei averages 110 nm, reaching a maximum of 250 nm (Fig. 4D and F). It is observed that a large proportion of those nuclei grow along surface features of the mineral electrode (e.g., grooves created from the polishing procedure). Fig. 5B shows depth profiles of the magnetite surface at − 450 and −650 mV across selected sections (the white lines in Fig. 4C and D). The heights of the U sorbates range between 35 and 70 nm at −450 mV and between 50 and 85 nm at −650 mV. Based on the size and height measurements in Figs. 3–5, the overall shape of the sorbates grown on ilmenite and magnetite can be described to be hemi-ellipsoidal.

Uranyl reduction in the presence of oxalate and EDTA was imaged with the mineral electrode before (Fig. 6A) and after sequential polarization at −250 and −450 mV for

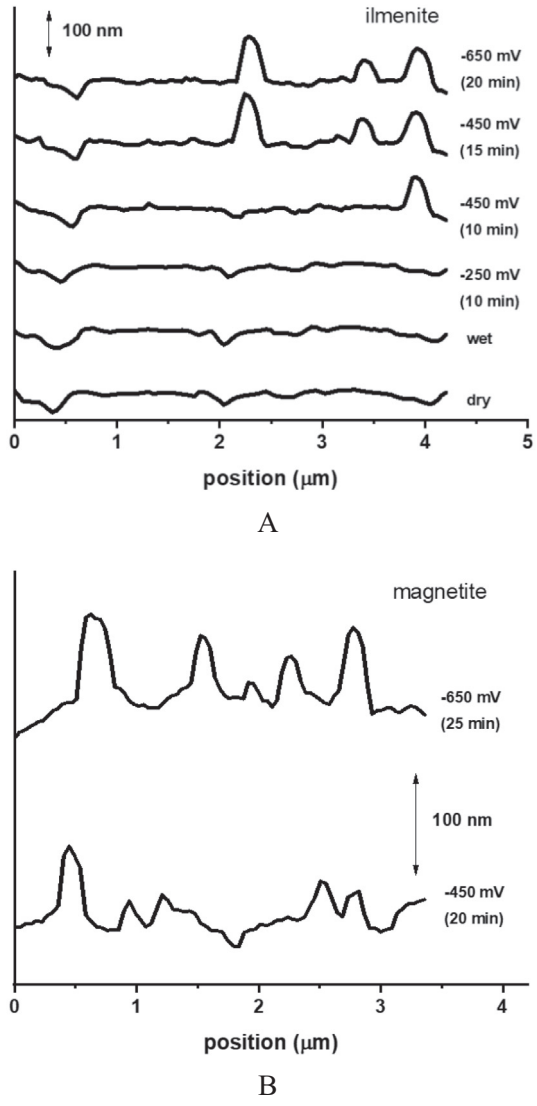


Fig. 5. (A) Changes in the topography of the ilmenite surface (across the white dashed line in Fig. 3F), showing the growth of U sorbates as a function of potential. (B) Depth profiles of U sorbates on magnetite at negative potentials (−450 and −650 mV) across different locations (the white lines in Fig. 4 C and D, respectively).

10 min at each potential (i.e., the total polarization time is 20 min; Fig. 6B–D). In the presence of oxalate, growth patterns of nuclei are comparable to those observed on uranyl reduction without organic ligands (Figs. 3 and 4), but with smaller volumes. The nuclei grown on magnetite and ilmenite with oxalate have an average diameter of 30 and 40 nm, respectively (Fig. 6B and C). In the presence of EDTA, the size of particles that grow on magnetite averages 30 nm (Fig. 6D).

3.3. Uranium oxidation state analysis using X-ray photoelectron spectroscopy (XPS)

XPS analysis was performed to measure the fractions of different U oxidation states resulting from the redox transformation mediated by magnetite and ilmenite. Samples for the analysis were prepared by sequentially applying potentials of −250 and −450 mV for 10 min at each potential step. XPS core scans of the U 4f peaks are presented in Fig. 7. Caution is taken to distinguish the different oxidation states of uranium (+IV, +V, and +VI) since their primary peaks split by spin–orbit coupling tend to overlap within a range of 3–4 eV. The corresponding U 4f satellite peaks appear at binding energies 4 to10 eV higher than the primary peaks. The binding energy separation ($\Delta E_{s\text{-}p}$) between the principal peak and the satellite one can be used because there is little or no overlap in $\Delta E_{s\text{-}p}$ values between the uranium oxidation states (Ilton and Bagus, 2011). Specifically, U(IV) and U(V) species typically display satellites at around 6 and 8 eV, respectively, above the primary U4f peaks, and the satellites that belong to U(VI) species appear at ~4 and ~10 eV above.

Based on the relationship between the primary peak and the satellite, we fit three components to the main peaks and satellites on the XPS spectra measured for uranyl reduction with and without oxalate and EDTA to discern uranium species with different oxidation states (Fig. 7). The fitting procedure documented by Ilton and Bagus (2011) is followed in this study. To be specific, we used identical primary peak shapes and full width at half maxima (FWHM) to assign the different oxidation states of uranium. Potential overlapping of nitrogen 1 s with U(V) $4f_{5/2}$ satellites at around 399 eV is considered in XPS peak assignment since uranyl nitrate was used to prepare U stock solution in this study (for more details, refer to Ilton and Bagus, 2011; Ilton et al., 2012). In all reaction samples of this study (i.e., reaction with and without oxalate and EDTA), the presence of U(V) is confirmed by the peak separations between the primary and satellite peaks ranging between 8.0 and 8.4 eV. No spectroscopic features indicating the presence of U(IV) are found (Fig. 7). The primary peaks appear at 381.5 ± 0.2 eV for U $4f_{7/2}$ and 392.4 ± 0.1 eV U$4f_{5/2}$ in case of U(VI) and $380.2 \pm 0.2/391.1 \pm 0.1$ eV for U(V) (Table 2). The values of U $4f_{7/2}$ observed in this study are consistent with the ones typically found in solid uranium phases (Ilton and Bagus, 2011). These XPS data reveal reduction of uranyl to U(V) species, in good agreement with the peak assignments on the cyclic voltammograms (Section 3.1).

The atomic ratio of U(V)/(total U) varies from 0.11 to 0.4 depending on reaction conditions and mineral substrates (Table 2). The ratio of U(V) to total U is found to be lower in the magnetite electrode reacted with U + EDTA than the ones with U only and U + oxalate. This change in ratios is likely due to higher fractions of uranyl species adsorbed on the surface in the presence of EDTA. That is, adsorption of negatively charged U(VI)-EDTA complexes (Table 1) would preferentially occur on the positively charged magnetite surface at pH 3 (the point of zero charge of magnetite is about 7; Tewari and McLean, 1972). Likewise, Kim et al. (2018) reported that U uptake by TiO_2 depends on the relation between the coexisting organic species and the surface charge.

Our XPS data indicate the formation of U(V) from the reduction of U(VI) mediated by magnetite and ilmenite in

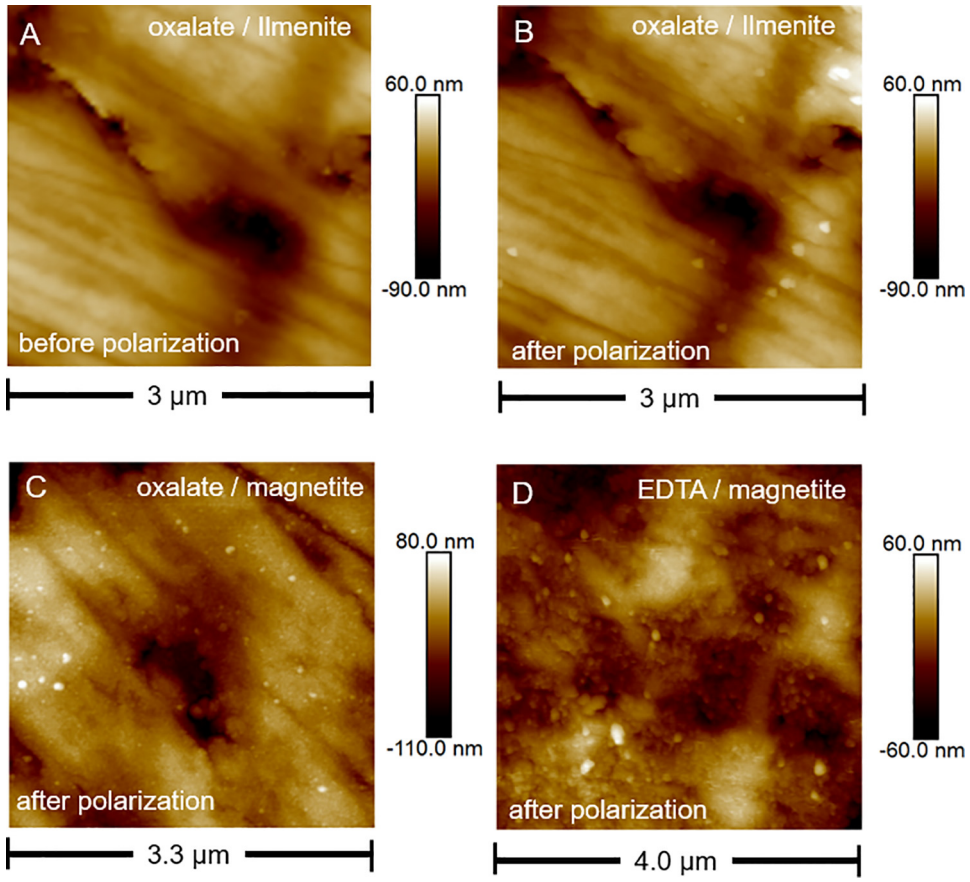


Fig. 6. EC-AFM height images of mineral electrodes (A) before and (B–D) after potentials of −0.25 and −0.45 V have been sequentially applied for 10 min at each potential (20 min of polarization). The electrode was a substrate of ilmenite and magnetite immersed in a solution with 0.3 mM uranyl and 0.3 mM of (A–C) oxalate and (D) EDTA at pH 3.0.

the absence and presence of oxalate and EDTA. The final products of this redox transformation are likely mixed-valence state U(VI/V) solids, as previously reported by Yuan et al. (2015a). However, the possibility of sorption of U(V)-organic complexes as a result of mineral-mediated reduction cannot be ruled out (e.g., Kim et al., 2018).

3.4. Quantum-mechanical calculations on the reduction potentials of uranyl-complexes

The reduction potential of uranyl is a good indicator of its tendency to be reduced in the environment. The complexation with organic molecules modifies the energetic state of uranyl, which causes a shift in the reduction potential. However, there are only limited data on thermodynamic quantities of U(VI/V) complexation with organic ligands (e.g., Hummel et al., 2005). We adopt density functional theory (DFT) calculation to theoretically estimate shifts in U(VI/V) reduction potentials by complexation with oxalate and EDTA. The calculated values indicate the thermodynamic favorability/unfavorability of redox transitions between hydrated organic-complexed U(VI/V) species (e.g., Eqs. (2) and (3)) relative to redox transformation between the hydrated water-bounded U(VI/V) species (Eq. (1)). By comparing calculated redox potentials with the ones obtained experimentally from CVs using magnetite and ilmenite electrodes, one can examine if the differences in complexation energies capture the nature of the observed shifts. Here, the equations needed to quantify a shift in redox potential are formulated, followed by the description of the structures and the energetics of the uranyl species relevant to our experiments.

The first step in the formulation is to relate the reduction of hydrated U(VI/V) species with the reduction of U(VI/V)-organic ligands. According to Hess's law, the energy required for the reduction of $U^{VI}O_2^{2+}$ to $U^{V}O_2^{+}$ (reaction A in Fig. 8) is independent of the route taken. One such route (route B comprising reaction B.1 to B.3 in Fig. 8) can proceed through the complexation of $U^{VI}O_2^{2+}$ with an organic compound $((U^{VI}O_2{\bullet}org)^{n+2}$ as a product; reaction B.1), the reduction of the complex to $(U^{V}O_2{\bullet}org)^{n+1}$ (reaction B.2), and the decomplexation to $U^{V}O_2^{+}$ (reaction B.3). Since the energies required for routes A and B are equal, the energy difference between reaction B.2 and A (here, defined as $\Delta(\Delta G_{cplx})$) is equivalent to the energy difference between the U^{V} complexation and U^{VI} complexation, which correspond to the reverse reaction of B.3 and the forward reaction of B.1, respectively. In turn, this quantity directly

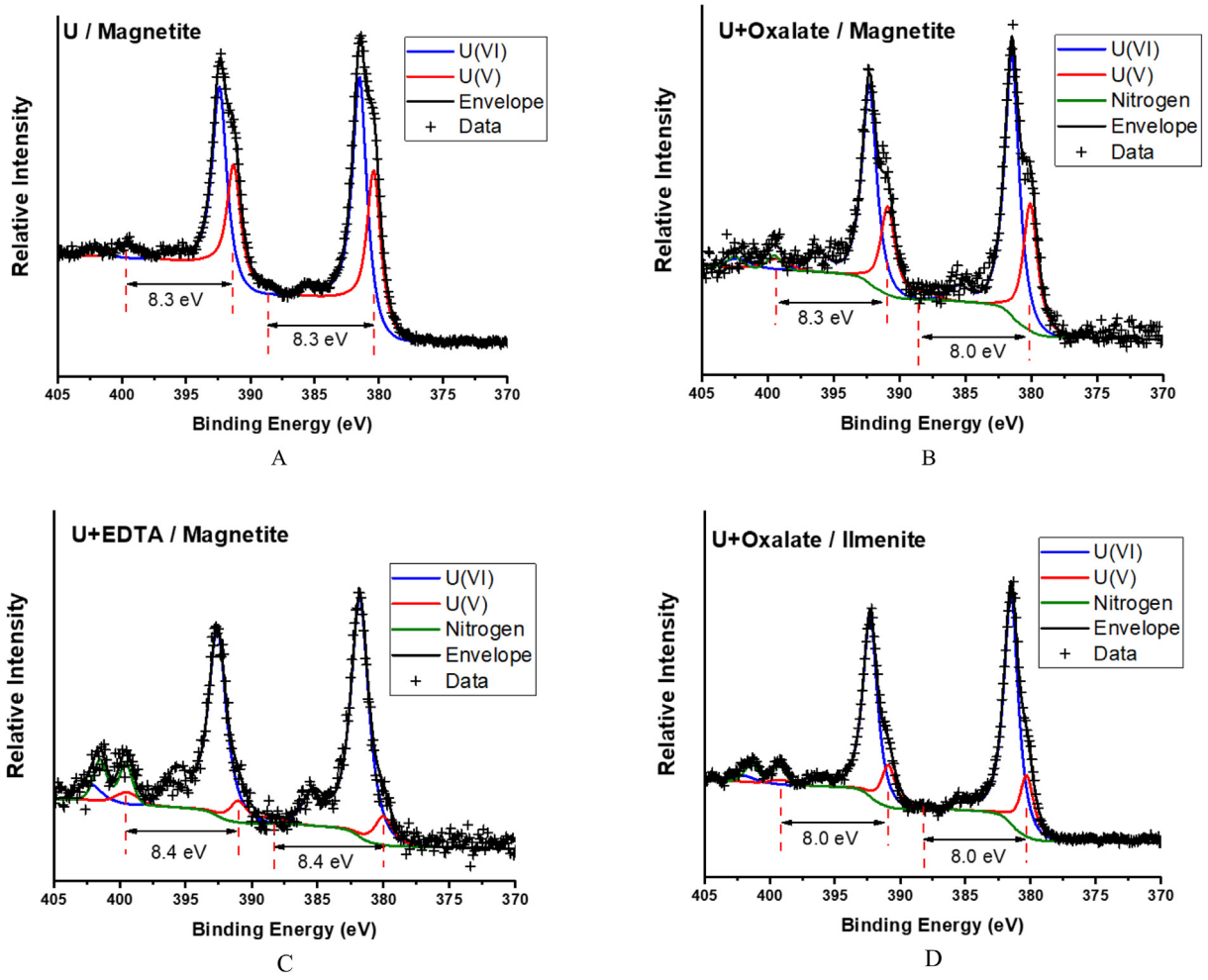


Fig. 7. Peak fits to the XPS spectra of U 4f orbitals for uranyl reduction mediated by magnetite (A) in the absence of organic ligands and in the presence of (B) oxalate and (C) EDTA, and (D) by ilmenite in the presence of oxalate.

Table 2
U 4f XPS results of uranyl reduction mediated by magnetite and ilmenite in the absence and presence of organic compounds.

		On magnetite		On ilmenite	
		U(VI)	U(V)	U(VI)	U(V)
U only	U4f7/2 (eV)	381.5	380.4	381.4	380.2
	U4f5/2 (eV)	392.4	391.3	392.3	391.1
	atomic fraction	0.6	0.4	0.76	0.24
U + oxalate	U4f7/2 (eV)	381.5	380.1	381.5	380.3
	U4f5/2 (eV)	392.3	390.9	392.30	391.10
	atomic fraction	0.68	0.32	0.8	0.2
U + EDTA	U4f7/2 (eV)	381.8	380.0		
	U4f5/2 (eV)	392.6	391.0		
	atomic fraction	0.89	0.11		

accounts for a shift in redox potential by complexation with an organic compound, as formulated by Eq. (4).

$$\Delta(\Delta G_{cplx}) = \Delta G^{Red}_{cplx} - \Delta G^{Ox}_{cplx} = -nF\Delta V \quad (4)$$

where ΔG^{Red}_{cplx} and ΔG^{Ox}_{cplx} are the Gibbs free energies of complexation of the reduced and oxidized uranyl species with an organic compound. The following reactions (Eqs. (5) and (6)) are the subtraction of reaction A (Eq. (1)) from

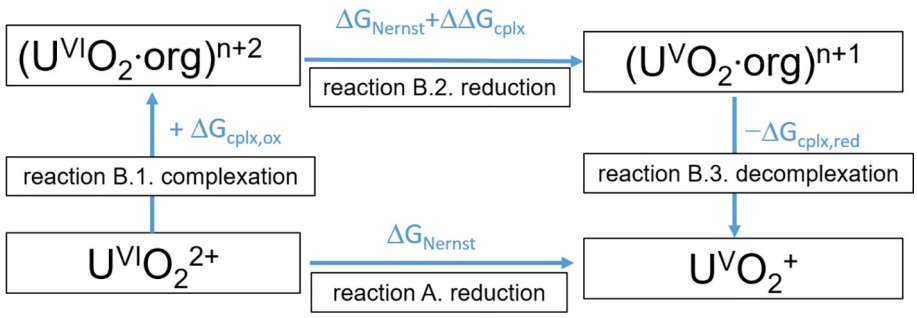


Fig. 8. Thermodynamic cycle diagram for the one-electron reduction of uranyl to conceptualize the shift in the reduction potential by complexation with organic species. Reaction A reflects the standard reduction potential of uranyl. Another route of uranyl reduction (route B) may proceed through organic complexation of U(VI) (reaction B.1), the one-electron reduction of organic-complexed U(VI) (B.2), and then decomplexation of organic complexed U(V) to form $U(V)O_2^+$ (B.3). The thermodynamic cycle is used to derive the reduction potential of organic-complexed uranyl: the difference in ΔG between the reduction of uranyl (reaction A) and organic-complexed uranyl (reaction B.2) equals the difference in ΔG of the complexation of hexavalent and pentavalent uranyl ($\Delta\Delta G_{cplx}$). By using Eq. (4) and the thermodynamic cycle, the peak shift (ΔV) by the complexation ($=\Delta\Delta G_{cplx}/(-F)$) can be calculated. The structure models of the aqueous and organic complexes are shown in Fig. 9.

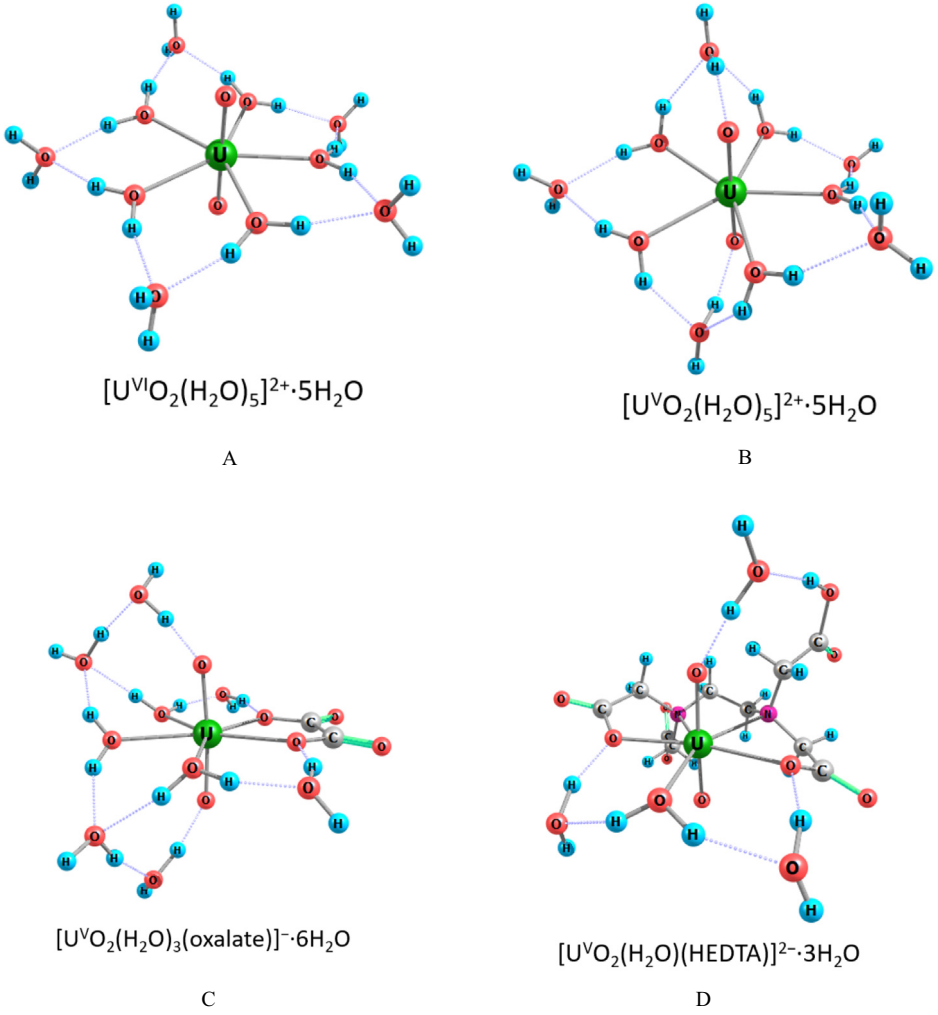


Fig. 9. Optimized structure of hydrated uranyl species; (A, B) uranyl in the oxidized and reduced form with U(VI) and U(V); (C, D) U(V)-oxalate and U(V)-EDTA complexes.

reaction B.2 (Eqs. (2) and (3)) derived for the one-electron transfer of U-oxalate and -EDTA species relevant to our experimental conditions:

$$(U^{VI}O_2{\cdot}\text{oxalate})^0 + U^{V}O_2^{+} \leftrightarrow (U^{V}O_2{\cdot}\text{oxalate})^{-} + U^{VI}O_2^{2+} \quad (5)$$

$$(U^{VI}O_2{\cdot}\text{HEDTA})^{-} + U^{V}O_2^{+} \leftrightarrow (U^{V}O_2{\cdot}\text{HEDTA})^{2-} + U^{VI}O_2^{2+} \quad (6)$$

In DFT modeling, the configurations of chemical species are built and subject to energy optimization. This modeling process provides information on the most stable structure of the chemical species and corresponding thermodynamic quantities. Hydration is a crucial modeling parameter to consider for simulating our experimental system where water is the reaction medium. For the hydrated uranyl ion, $U^{VI}O_2^{2+}$, five water molecules are coordinated in the equatorial plane of the central uranium atom while the two O atoms of the uranyl ion are axially aligned (Fig. 9A). The equatorial water molecules tend to form strong hydrogen bonding with extra waters, which can be properly described by the second water shell on the equatorial plane. Since the axial O atoms of uranyl do not strongly interact with water molecules, no other explicit water molecules are introduced. When the reduced form of uranyl, $U^{V}O_2^{+}$, is subject to energy optimization, two water molecules in the second water shell are relocated to form H bonding with the two axial O atoms (Fig. 9B). These optimization results are consistent with the structures of hydrated U(VI/V) molecules with five additional water molecules reported by Shamov and Schreckenbach (2005). The initial structure of the U(VI)-oxalate 1:1 complex $(U^{VI}O_2{\cdot}\text{oxalate})^0$ was modified from Tsushima et al. (2010), which involves U-oxalate binding in a bidentate mode and three water molecules forming the first coordination shell. Compared to their model, we consider the second water shell around the equatorial water molecules and the axial O atoms. The initial configuration of U(V)-oxalate 1:1 complex, $(U^{V}O_2{\cdot}\text{oxalate})^{-}$ was the same as the one of U(VI)-oxalate 1:1 complex but with a charge of −1 and a spin multiplicity of 2. The optimized structure of the U(V)-oxalate complex is displayed in Fig. 9C. For the uranyl-EDTA complex, the uranyl molecule binds to $HEDTA^{3-}$ through two amines and two carboxylates and to one extra water molecule on the equatorial positions (Fig. 9D).

The calculation results reveal the thermodynamic values of corresponding species and are summarized in Table 3. The electronic energies corrected for hydration are 2.5 and 20.9 kJ/mol for the one-electron exchange processes with U(VI/V)-oxalate species and U(VI/V)-EDTA species (Eqs. (5) and (6)), respectively. The calculated Gibbs free energies of Eqs. (5) and (6) are 9.9 and 36.9 kJ/mol, respectively. These positive electronic and Gibbs free energies indicate that the reactants are energetically more stable than the products. Therefore, the reduction of hydrated UO_2^{2+} is more energetically favorable than that of the organic-complexed UO_2^{2+} species. The net effect of complexation with these organic ligands would be, therefore, a thermodynamic shift towards more negative redox potentials of the U(VI/V) transition. These calculated values of changes in Gibbs free energies (Table 3) correspond to reduction potential shifts of U(VI/V) redox transformation by complexation with oxalate by −0.10 V and with EDTA by −0.38 V as estimated from Eq. (4).

These computational results coincide with the electrochemical observation that the reduction potential of uranyl measured on the magnetite surface is 80 mV lower in the presence of oxalate compared to the reduction potential measured without organic ligands (Fig. 1A and B). It is inferred that the uranyl-oxalate 1:1 complex is a redox-active species undergoing redox transformation mediated by magnetite. The computational prediction indicates a shift in reduction potential by a few hundred mV if the redox reactions occur in the form of uranyl-EDTA complexes. No apparent shift in reduction potential is found from the CV of uranyl measured with the magnetite electrode in the presence of a 1:1 of U to EDTA ratio, indicating minimal contributions of U-EDTA complexes to the reduction potential measured in this solution. U-EDTA complexes could undergo decomplexation via interaction with the surface functional groups prior to magnetite-mediated redox reactions. This possibility is further discussed in Section 4.1.

4. DISCUSSION

4.1. Uranyl reduction mechanisms as mediated by Fe-bearing minerals

Our results of AFM imaging and electrochemistry experiments demonstrate that one-electron transfer

Table 3
Computational results of thermodynamics of uranyl complexations compared with experimental data.

Complexation reactions	Computational				Experimental**
	Δ (E + Hyd)* (kJ/mol)	ΔH (kJ/mol)	ΔS (J/(mol K))	ΔG (kJ/mol)	ΔG (kJ/mol)
$(U^{VI}O_2{\cdot}\text{oxalate})^0 + U^{V}O_2^{+} \leftrightarrow (U^{V}O_2{\cdot}\text{oxalate})^{-} + U^{VI}O_2^{2+}$	2.5	7.9	−6.8	9.9 (0.10 eV)	11.4
$(U^{VI}O_2{\cdot}\text{HEDTA})^0 + U^{V}O_2^{+} \leftrightarrow (U^{V}O_2{\cdot}\text{HEDTA})^{-} + U^{VI}O_2^{2+}$	20.9	29.2	−25.9	36.9 (0.38 eV)	—

* Electronic energy calculated with the conductor-like polarizable continuum model (CPCM) (see the methods section for more details).
** Inferred from the stability constants of aqueous U(VI) oxalate ($UO_2^{2+} + \text{oxalate}^{2-} \leftrightarrow (UO_2{\cdot}\text{oxalate})^0$; log K = 6.0) and U(V) oxalate ($UO_2^{+} + \text{oxalate}^{2-} \leftrightarrow (UO_2{\cdot}\text{oxalate})^{-}$; log K = 4.0) from Ferri et al. (2000) and Moskvin (1971), respectively, both of which are compiled in Hummel et al. (2005).

between hydrated U(VI/V) species is mediated by magnetite and ilmenite, giving rise to heterogeneous reduction precipitates, likely in the form of mixed-valance U(VI/V) solids. In the presence of oxalate at a 1:1 U to oxalate ratio, uranyl-oxalate complexes can be reduced to forms with the oxidation state of V as mediated by magnetite. At the same uranyl to EDTA ratio where uranyl-EDTA complexes are expected to dominate in solution, the reduction of uranyl seems to occur in the form of hydrated uranyl without complexation. Uranyl-EDTA complexes may break into uranyl and EDTA to form new complexes while interacting with surface-bound Fe(II/III) on magnetite (Eq. (7)).

$$(U^{VI}O_2{\cdot}HEDTA)^- + Fe^{2+/3+}\ (\text{surface-bounded Fe}) \leftrightarrow U^{VI}O_2^{2+} + (Fe^{2+/3+}EDTA)^{-/2-} + H^+ \quad (7)$$

To further examine this possibility, CV was measured with magnetite at a 1:1 molar ratio of Fe to EDTA (Fig. 1D). This measurement reveals a peak pair with a midpoint potential of 0.07 V, corresponding to a one-electron transfer between Fe(II/III)-EDTA species (Eq. (8)).

$$(Fe^{III}{\cdot}EDTA)^- + e^- \leftrightarrow (Fe^{II}{\cdot}EDTA)^{2-} \quad (8)$$

This peak pair matches the one that appears on the background CV curve measured in a solution containing EDTA without U and Fe (the baseline in Fig. 1D). This is evidence for the strong interaction of surface-bound Fe with EDTA. At a 1:1 uranyl to EDTA ratio (Fig. 1C), a broad shoulder appears on anodic scanning with magnetite, whose position is in agreement with the anodic peak of this Fe-EDTA redox reaction (0.13 V). U-EDTA species could undergo decomplexation while interacting with the magnetite surface, which results in Fe-EDTA species and hydrated uranyl. In turn, the presence of hydrated uranyl at the magnetite-water interface can explain the absence of a shift in the uranyl reduction potential on the CV measurement at a 1:1 ratio of uranyl to EDTA.

4.2. Geochemical and environmental implications

The reduction of soluble uranyl into immobile forms is an important process in the global uranium cycle. Understanding the mechanisms of the reduction process is also an important step in developing broadly applicable techniques for removing uranium from contaminated environments. This study has shed light on uranyl reduction mediated by naturally occurring Fe oxide minerals. Owing to their semiconducting properties, magnetite and ilmenite can catalyze electron transfer between adsorbed uranyl as an oxidant and other inorganic (e.g., Fe(II); Taylor et al., 2017b) and organic species as a reductant.

The electrochemical and spectroscopic data of this study demonstrate that the transition of U(VI) to U(V) is the main reaction step upon uranyl reduction mediated by magnetite and ilmenite. Our AFM images of uranyl reduction on the mineral surface indicate immobilization of U (VI/V) in solid forms. These results are consistent with previous studies that have reported the formation of U(V) from heterogeneous uranyl reduction involving Fe-bearing minerals (e.g., pyrite, hematite, and magnetite; Ilton et al., 2012; Renock et al., 2013; Yuan et al., 2015b). Predictions for the long-term immobilization of uranium is beyond the scope of the present study. Yet, the mineral-mediated formation of U(V) could be an initial step in long-lasting reaction sequences involving uranyl species in subsurface environments where iron oxide and sulfide minerals are abundant. This step could be followed by kinetically slow U(V) disproportion (Eq. (9)) that leads to the formation of U(IV) species and U(IV)-containing minerals like uraninite.

$$2UO_2^+ \leftrightarrow UO_2^{2+} + UO_2^0 \quad (9)$$

This study provides new insights into the interplay between organic ligands and Fe minerals upon uranyl reduction. Uranyl-organic complexes may be redox-active in mineral-mediated reduction, as demonstrated from redox transformation of U(VI/V)-oxalate complexes. Yet, complexation with organic ligands could lower the thermodynamic spontaneity of uranyl as indicated by our computational results (i.e., indicated by negative shifts in reduction potential of uranyl). The surface-bound Fe on fresh mineral surfaces can preferentially bond with organic ligands like EDTA, which can be conducive to decomplexation of uranyl and thus facilitate the reduction of uranyl in the hydrated form.

5. CONCLUSIONS

The results of this study advance our understanding of reaction mechanisms and pathways of the uranyl reduction and nucleation mediated by magnetite and ilmenite. The mineral-mediated metal reduction and growth processes were *in situ* visualized at nanoscales, while electron transfer reaction steps were identified from electrochemical measurements. To the authors' knowledge, this study is the first to identify redox features evidencing the reduction of U(VI) to U(V) on ilmenite and the reduction of the 1:1 U(VI)-oxalate complex to the 1:1 U(V)-oxalate complex on magnetite. Quantum mechanical calculations predict from one to a few hundred mV shifts in the reduction potential of uranyl by organic complexation. This information is useful to evaluate the redox reactivity of uranyl in reaction systems involving organic compounds. Our experimental and computational results demonstrate that the catalysis of redox transformations occurring at the mineral surface is critical in evaluating the fate and mobility of uranium in the environments. The methodology used in this study, combining electrochemical, microscopic, and computational approaches, has broad applications and enables future studies to quantify redox reaction pathways and mechanisms for other redox-sensitive species.

Some open questions remain about the mineralogy of the U sorbates and the Fe oxide substrates. Yuan et al. (2015a) investigated the reduction of U(VI) to U(V) mediated by magnetite in the absence of organic species and suggested that the U(VI/V) precipitates are likely to be structurally disordered due to high water contents

in the structure. Systematic investigations are needed to address the stability, crystallinity, and water content of U(VI/V) sorbates grown on the Fe-bearing minerals, which could depend on coexisting organic species. Although the scope of this study has focused on the U redox transformation mediated by bulk magnetite and ilmenite, the redox behavior of uranyl may depend on particular facets (or cleavage planes) of the minerals (e.g., magnetite (0 0 1) versus (1 1 1) surfaces). Therefore, comparison in the U reduction reactions between different mineral facets would be an interesting topic for future study.

6. RESEARCH DATA

Research data to this article can be found online at https://doi.org/10.7302/mf7d-bw87.

Declaration of Competing Interest

The authors declare that they have no known competing financial interests or personal relationships that could have appeared to influence the work reported in this paper.

ACKNOWLEDGEMENTS

The authors are grateful for the support from the U.S. Department of Energy's (DOE) Office of Science, 464 Office of Basic Energy Sciences (BES), Chemical Sciences, Geosciences, & Biosciences (CSGB) Division 465 for the topics of Heavy Element Chemistry and Geoscience (grant number DE-FG02-06ER15783). Y.K. acknowledges support from Samsung Scholarship.

REFERENCES

Becker U., Risthaus P., Bosbach D. and Putnis A. (2002) Selective attachment of monovalent background electrolyte ions and growth inhibitors to polar steps on sulfates as studied by molecular simulations and AFM observations. *Mol. Simul.* **28**, 607–632.

Bergner A., Dolg M., Küchle W., Stoll H. and Preuß H. (1993) Ab initio energy-adjusted pseudopotentials for elements of groups 13–17. *Mol. Phys.* **80**, 1431–1441.

Campbell J., Stromatt R., Smith M., Bean R., Jones T. and Strachan D. (1994) Organic analysis at the Hanford nuclear site. *Anal. Chem.* **66**, 1208A–1215A.

Charlet L., Bosbach D. and Peretyashko T. (2002) Natural attenuation of TCE, As, Hg linked to the heterogeneous oxidation of Fe (II): an AFM study. *Chem. Geol.* **190**, 303–319.

Djogić R. and Branica M. (1993) Study of uranyl (VI) ion reduction at various ionic strengths of sodium perchlorate. *Anal. Chim. Acta* **281**, 291–297.

Ferri D., Iuliano M., Manfredi C., Vasca E., Caruso T., Clemente M. and Fontanella C. (2000) Dioxouranium (VI) oxalate complexes. *J. Chem. Soc., Dalton Trans.*, 3460–3466.

Gadd G. M. (1999) Fungal production of citric and oxalic acid: importance in metal speciation, physiology and biogeochemical processes. *Adv. Micro. Physiol. Elsevier*, 47–92.

Gillson J. L. (1932) Genesis of the ilmenite deposits of Saint Urbain, County Charlevoix, Quebec. *Econ. Geol.* **27**, 554–577.

Havel J., Soto-Guerrero J. and Lubal P. (2002) Spectrophotometric study of uranyl–oxalate complexation in solution. *Polyhedron* **21**, 1411–1420.

Hemmersam A. G., Rechendorff K., Besenbacher F., Kasemo B. and Sutherland D. S. (2008) pH-dependent adsorption and conformational change of ferritin studied on metal oxide surfaces by a combination of QCM-D and AFM. *J. Phys. Chem. C* **112**, 4180–4186.

Hixon A. E., Hu Y.-J., Kaplan D., Kukkadapu R. K., Nitsche H., Qafoku O. and Powell B. A. (2010) Influence of iron redox transformations on plutonium sorption to sediments. *Radiochim. Acta* **98**, 685–692.

Hummel W., Mompean F. J., Illemassène M. and Perrone J. (2005) *Chemical thermodynamics of compounds and complexes of U, Np, Pu, Am, Tc, Se, Ni and Zr with selected organic ligands*. Elsevier, Amsterdam.

Ilton E. S. and Bagus P. S. (2011) XPS determination of uranium oxidation states. *Surf. Interface Anal.* **43**, 1549–1560.

Ilton E. S., Boily J.-F. and Bagus P. S. (2007) Beam induced reduction of U (VI) during X-ray photoelectron spectroscopy: the utility of the U4f satellite structure for identifying uranium oxidation states in mixed valence uranium oxides. *Surf. Sci.* **601**, 908–916.

Ilton E. S., Pacheco J. S. L., Bargar J. R., Shi Z., Liu J., Kovarik L., Engelhard M. H. and Felmy A. R. (2012) Reduction of U (VI) incorporated in the structure of hematite. *Environ. Sci. Technol.* **46**, 9428–9436.

Iwasawa Y., Onishi H., Fukui K.-I., Suzuki S. and Sasaki T. (1999) The selective adsorption and kinetic behaviour of molecules on TiO_2 (110) observed by STM and NC-AFM. *Faraday Discuss.* **114**, 259–266.

Karlsson P. M., Anderson M. W. and Palmqvist A. E. (2010) Adsorption of sodium dodecyl sulfate and sodium dodecyl phosphate at the surface of aluminium oxide studied with AFM. *Corros. Sci.* **52**, 1103–1105.

Kim Y., Marcano M. C., Ellis B. R. and Becker U. (2018) Photocatalytic reduction of uranyl: effects of organic ligands and UV light wavelengths. *Am. J. Sci.* **318**, 949–968.

Kim Y., Seo J., Kang S.-A., Choi S.-G. and Lee Y. J. (2015) Geochemistry and uranium mineralogy of the black slate in the Okcheon Metamorphic Belt, South Korea. *Geochem. J.* **49**, 443–452.

Lee C., Yang W. and Parr R. G. (1988) Development of the Colle-Salvetti correlation-energy formula into a functional of the electron density. *Phys. Rev. B* **37**, 785.

Lovley D. R. (1993) Dissimilatory metal reduction. *Annu. Rev. Miicrobiol.* **47**, 263–290.

Moskvin A. (1971) Correlation of the stability constants of complexes of the actinides with the properties of the metal ions and ligand forming them. *Sov. Radiochem.* **13**, 230–237.

O'Loughlin E. J., Kelly S. D., Cook R. E., Csencsits R. and Kemner K. M. (2003) Reduction of uranium (VI) by mixed iron (II)/iron (III) hydroxide (green rust): formation of UO_2 nanoparticles. *Environ. Sci. Technol.* **37**, 721–727.

Pan Z., Li W., Fortner J. D. and Giammar D. E. (2017) Measurement and surface complexation modeling of U (VI) adsorption to engineered iron oxide nanoparticles. *Environ. Sci. Technol.* **51**, 9219–9226.

Pina C., Putnis C. V., Becker U., Biswas S., Carroll E., Bosbach D. and Putnis A. (2004) An atomic force microscopy and molecular simulations study of the inhibition of barite growth by phosphonates. *Surf. Sci.* **553**, 61–74.

Pina C. M., Becker U., Risthaus P., Bosbach D. and Putnis A. (1998) Molecular-scale mechanisms of crystal growth in barite. *Nature* **395**, 483–486.

Powell B. A., Fjeld R. A., Kaplan D. I., Coates J. T. and Serkiz S. M. (2004) $Pu(V)O^{2+}$ adsorption and reduction by synthetic magnetite (Fe_3O_4). *Environ. Sci. Technol.* **38**, 6016–6024.

Renock D., Mueller M., Yuan K., Ewing R. C. and Becker U. (2013) The energetics and kinetics of uranyl reduction on pyrite, hematite, and magnetite surfaces: a powder microelectrode study. *Geochim. Cosmochim. Acta* **118**, 56–71.

Risthaus P., Bosbach D., Becker U. and Putnis A. (2001) Barite scale formation and dissolution at high ionic strength studied with atomic force microscopy. *Colloids Surf. A* **191**, 201–214.

Shamov G. A. and Schreckenbach G. (2005) Density functional studies of actinyl aquo complexes studied using small-core effective core potentials and a scalar four-component relativistic method. *J. Phys. Chem. A* **109**, 10961–10974.

Sun Y., Li J. and Wang X. (2014) The retention of uranium and europium onto sepiolite investigated by macroscopic, spectroscopic and modeling techniques. *Geochim. Cosmochim. Acta* **140**, 621–643.

Taylor S., Becker U. and Rosso K. (2017a) Electron transfer pathways facilitating U (VI) reduction by Fe (II) on Al-vs Fe-oxides. *J. Phys. Chem. C* **121**, 19887–19903.

Taylor S., Marcano M. and Becker U. (2017b) A first principles investigation of electron transfer between Fe (II) and U (VI) on insulating Al-vs. semiconducting Fe-oxide surfaces via the proximity effect. *Geochim. Cosmochim. Acta* **197**, 305–322.

Taylor S., Marcano M., Rosso K. M. and Becker U. (2015) An experimental and ab initio study on the abiotic reduction of uranyl by ferrous iron. *Geochim. Cosmochim. Acta* **156**, 154–172.

Tewari P. and McLean A. (1972) Temperature dependence of point of zero charge of alumina and magnetite. *J. Colloid Interf. Sci.* **40**, 267–272.

Tsushima S., Brendler V. and Fahmy K. (2010) Aqueous coordination chemistry and photochemistry of uranyl (VI) oxalate revisited: a density functional theory study. *Dalton Trans.* **39**, 10953–10958.

Ulrich K.-U., Ilton E. S., Veeramani H., Sharp J. O., Bernier-Latmani R., Schofield E. J., Bargar J. R. and Giammar D. E. (2009) Comparative dissolution kinetics of biogenic and chemogenic uraninite under oxidizing conditions in the presence of carbonate. *Geochim. Cosmochim. Acta* **73**, 6065–6083.

Walker S. M., Marcano M. C., Bender W. M. and Becker U. (2016) Imaging the reduction of chromium (VI) on magnetite surfaces using in situ electrochemical AFM. *Chem. Geol.* **429**, 60–74.

Wersin P., Hochella, Jr, M. F., Persson P., Redden G., Leckie J. O. and Harris D. W. (1994) Interaction between aqueous uranium (VI) and sulfide minerals: spectroscopic evidence for sorption and reduction. *Geochim. Cosmochim. Acta* **58**, 2829–2843.

White A. F., Peterson M. L. and Hochella, Jr, M. F. (1994) Electrochemistry and dissolution kinetics of magnetite and ilmenite. *Geochim. Cosmochim. Acta* **58**, 1859–1875.

Xu Y. and Schoonen M. A. (2000) The absolute energy positions of conduction and valence bands of selected semiconducting minerals. *Am. Mineral.* **85**, 543–556.

Yang S., Li Q., Chen L., Chen Z., Hu B., Wang H. and Wang X. (2020) Synergistic removal and reduction of U (VI) and Cr (VI) by Fe_3S_4 micro-crystal. *Chem. Eng. J.* **385**, 123909.

Yuan K., Ilton E. S., Antonio M. R., Li Z., Cook P. J. and Becker U. (2015a) Electrochemical and spectroscopic evidence on the one-electron reduction of U (VI) to U (V) on magnetite. *Environ. Sci. Technol.* **49**, 6206–6213.

Yuan K., Renock D., Ewing R. C. and Becker U. (2015b) Uranium reduction on magnetite: probing for pentavalent uranium using electrochemical methods. *Geochim. Cosmochim. Acta* **156**, 194–206.

Associate editor: Annie B. Kersting